



LAWRENCE
LIVERMORE
NATIONAL
LABORATORY

Implementation of a generalized actuator disk wind turbine model into the Weather Research and Forecasting Model for large-eddy simulation applications

J. D. Mirocha, B. Kosovic, M. L. Aitken, J. K. Lundquist

June 26, 2013

Journal of Renewable and Sustainable Energy

Disclaimer

This document was prepared as an account of work sponsored by an agency of the United States government. Neither the United States government nor Lawrence Livermore National Security, LLC, nor any of their employees makes any warranty, expressed or implied, or assumes any legal liability or responsibility for the accuracy, completeness, or usefulness of any information, apparatus, product, or process disclosed, or represents that its use would not infringe privately owned rights. Reference herein to any specific commercial product, process, or service by trade name, trademark, manufacturer, or otherwise does not necessarily constitute or imply its endorsement, recommendation, or favoring by the United States government or Lawrence Livermore National Security, LLC. The views and opinions of authors expressed herein do not necessarily state or reflect those of the United States government or Lawrence Livermore National Security, LLC, and shall not be used for advertising or product endorsement purposes.

Implementation of a Generalized Actuator Disk Wind Turbine Model into the Weather Research and Forecasting Model for Large-Eddy Simulation Applications

J.D. Mirocha,^{1a)} B. Kosovic,² M.L. Aitken,³ and J.K. Lundquist^{4,5}

¹Lawrence Livermore National Laboratory, 7000 East Avenue, Livermore, California, 94551, USA

²National Center for Atmospheric Research, P.O. Box 3000, Boulder, Colorado, 80307 USA

³Department of Physics, University of Colorado at Boulder, 390 UCB, Boulder, Colorado, 80309-0390, USA

⁴Department of Atmospheric and Oceanic Sciences, University of Colorado at Boulder, 311 UCB, Boulder, Colorado, 80309-0311 USA

⁵National Renewable Energy Laboratory, 15013 Denver West Parkway, Golden, Colorado, 80401-3305, USA

^{a)} Email: jmirocha@llnl.gov

Abstract. A generalized actuator disk (GAD) wind turbine parameterization designed for large-eddy simulation (LES) applications was implemented into the Weather Research and Forecasting (WRF) model. WRF-LES with the GAD model enables numerical investigation of the effects of an operating wind turbine on and interactions with a broad range of atmospheric boundary layer phenomena. Numerical simulations using WRF-LES with the GAD model were compared with measurements obtained from the Turbine Wake and Inflow Characterization Study (TWICS-2011), the goal of which was to measure both the inflow to and wake from a 2.3-MW wind turbine. Data from a meteorological tower and two light-detection and ranging (lidar) systems, one vertically profiling and another operated over a variety of scanning modes, were utilized to obtain forcing for the simulations, and to evaluate characteristics of the simulated wakes. Simulations produced wakes with physically consistent rotation and velocity deficits. Two surface heat flux values of 20 W m^{-2} and 100 W m^{-2} were used to examine the sensitivity of the simulated wakes to convective instability. Simulations using the smaller heat flux values showed good agreement with wake deficits observed during TWICS-2011, whereas those using the larger value showed enhanced spreading and more-rapid attenuation. This study demonstrates the utility of actuator models implemented within atmospheric LES to address a range of atmospheric science and engineering applications. Validated implementation of the GAD in a numerical weather prediction code such as WRF will enable a wide range of studies related to the interaction of wind turbines with the atmosphere and surface.

I. INTRODUCTION

Wind turbines operate within the atmospheric boundary layer (ABL), the turbulent layer of the atmosphere adjacent to the surface. Turbulence is of particular importance to wind energy, having been identified as a key modulator of both power production^{1,2,3} and fatigue loading,^{4,5,6,7} which impacts the reliability, maintenance, and life spans of various turbine components.⁷

Although turbulence is a characteristic feature of the ABL, variations in turbulence structure and dynamics are notoriously difficult to predict. Mesoscale weather prediction models utilize grids that are too coarse to resolve the turbulence directly; instead, the effects of unresolved turbulence on mean quantities are parameterized in a subgrid-scale planetary boundary layer parameterization. Such parameterizations can represent basic processes using bulk properties of ABLs, but do not provide detailed information about the subgrid-scale turbulence processes that can impact wind turbines in important ways.

Computational fluid dynamic models, which do employ sufficient grid spacing to resolve the large and energetically important scales of turbulence directly, generally do not contain models for important atmospheric physical processes that modulate turbulence dynamics.⁸ These include the transfer of solar and terrestrial radiation between the surface and the atmosphere, formation and evolution of cloud and microphysical properties, and surface interactions, including the exchange of radiation as well as sensible and latent heat. The limitations of computational fluid dynamic models can be overcome through coupling with numerical weather prediction models such as WRF.⁹ However, coupling introduces new complexity via differences in numerical solution methods, grid structures, and subgrid parameterizations.

The structure and dynamics of the ABL can vary considerably over the diurnal cycle and under varying meteorological conditions. Although convective cells or rolls are often observed during unstable conditions, stable conditions frequently feature strong shear and intermittent turbulence associated with Kelvin-Helmholtz waves.^{10,11,12} Given the considerable impacts of atmospheric turbulence on wind turbine performance and fatigue loading,¹³ a capability to realistically simulate turbulence over the diurnal cycle and under varying meteorology stands as a critical need for a variety of wind energy research applications.

Wind turbines, in turn, generate wakes, disturbances to the flow characterized by velocity deficits and increased turbulence levels.^{14,15} A recent experimental study^{16,17} and several numerical simulations^{18,19} have demonstrated that wind turbine wakes can persist for significant distances downstream. Power losses of up to 40% have been observed in downstream turbines in large arrays as a result of wakes from upstream turbines.² In addition to power losses, elevated turbulence levels occurring in wakes have been implicated in accelerated fatigue of turbine components, specifically gearboxes, increasing maintenance frequency and shortening operational life spans.^{7,18} Increases of turbulence intensities of up to 50% beyond their background values have been measured at distances of 10 rotor diameters downstream of large turbines.²⁰ In addition, it has been suggested that persistent velocity deficits and increased turbulence levels in aggregated wakes emanating from large wind projects may influence not only the performance of neighboring wind projects,²¹ but also affect surface exchange process, potentially impacting crop growth and other ecosystem dynamics.^{22,23}

Turbine wakes interact with ABL turbulence in a manner that is varied and often poorly understood, complicating characterization and methods for assessment, prediction, or mitigation. A lack of appropriate data sets that include both inflow and wake parameters hinders

construction of a detailed conceptual understanding. Likewise, contemporary computational frameworks are still working toward capturing realistic turbine/atmosphere interactions, especially during changing weather conditions. Although Churchfield et al.²⁴ have simulated wind turbine arrays using the OpenFOAM solver, and Lee et al.²⁵ and Fleming et al.²⁶ have coupled aerodynamics and structural response models and wind plant control modules—each important steps toward an integrated approach to wind turbine modeling—these frameworks still require realistic atmospheric inflow for real-world applications.

To address the need for a computational framework capable of capturing atmosphere/turbine interactions in a realistic ABL environment, a generalized actuator disk (GAD) model appropriate for large-eddy simulation (LES) applications was implemented within the Weather Research and Forecasting (WRF) model. WRF is a fully compressible non-hydrostatic atmospheric model²⁷ that, although used primarily for mesoscale applications, also supports an LES option that has been validated in a range of atmospheric conditions.^{28,29,30,31,32,33}

Although WRF currently features a mesoscale wind farm wake parameterization, that model is designed for mesoscale applications, for which turbine effects are aggregated within the footprint of grid cells with horizontal dimensions larger than the turbine rotor disk.³⁴ The effects of turbines are parameterized as elevated drag, which reduces mean wind speed, and enhanced subgrid turbulence kinetic energy (TKE), which modulates ABL dynamics and mixing processes via enhanced diffusion. Crucially, this parameterization is designed for large-scale simulations of wind farm impacts, and, although capable of quantifying wind farm impacts in a range of stability conditions, is not designed to work at fine enough scales to include interactions with resolved-scale turbulence.³⁵ Resolution of such interactions is critical to forming a clearer

understanding of how turbines respond to and interact with ABL turbulence, structure, and dynamics, and how the modified ABL evolves downstream.

The LES technique explicitly resolves the largest scales of three-dimensional atmospheric turbulence, those responsible for most of the turbulent transport and turbulence kinetic energy production. Smaller scales of motion, which function primarily to dissipate energy from the resolved scales, are modeled in a subgrid (or subfilter) scale stress model.^{36,37,38} LES can therefore capture both key turbulence phenomena within the ABL and their interactions with wind turbines via incorporation of a GAD.

The fidelity of simulated turbulence/turbine interactions is governed by the resolution of the LES, the effectiveness and accuracy of the subgrid turbulence parameterization, and the specifics of the wind turbine model. For LES of the ABL, the forces applied to the flow by the presence of wind turbines can be approximated to a high degree using a GAD.^{39,40} The GAD represents the turbine as a two-dimensional disk containing the rotating turbine, with forces on both the disk and the atmosphere computed by combining analysis of momentum balance in rotating, annular rings intersecting the disk, with lift and drag forces computed along isolated, two-dimensional blade elements, using two-dimensional aerodynamic theory. The GAD requires sufficient mesh resolution that several computational grid points in each direction are contained within the turbine's rotor swept area.

The GAD model implemented into WRF follows the generalization of the Blade Element Momentum theory of Glauert⁴¹ by Madsen⁴², Sørensen et al.⁴³, Sørensen and Mikkelsen,⁴⁴ and Mikkelsen.³⁹ The GAD computes both drag and rotation forces. Although the drag force is primarily responsible for the reduction in flow speed in the wake, rotation has important impacts

on kinetic energy transport.⁴⁵ Further details about implementation of the GAD into WRF can be found in the appendix.

Motivations for implementing a GAD model within the WRF framework include WRF's full suite of physical process models, which can provide realistic forcing for the ABL, and a grid nesting capability, whereby portions of a model domain can be simulated at a higher resolution, with lateral boundary conditions for the nested domain(s) provided by the outer domain(s). Such an approach permits a fine-scale LES domain with one or several GAD model(s) to be nested within a coarser, bounding LES, a procedure that can straightforwardly and efficiently provide turbulent inflow (and outflow) conditions for the nested domain. Furthermore, the nesting approach can be extended to provide the LES domain(s) with mesoscale inflow, potentially providing the LES with realistic, time-varying lateral boundary conditions, containing both mesoscale features and resolved-scale ABL turbulence. A growing community of WRF developers is constructing algorithms and guidelines to support such downscaling efforts.^{30,46,47} WRF supports two options for nesting, both one-way, for which the bounding domain receives no information from a domain nested within it, and two-way nesting, for which the nested domain solution influences the bounding domain. The flexibility of the WRF framework, combined with a GAD parameterization, can potentially support a wide range of applications involving airflow/turbine interactions in both idealized and real-world setups.

II. MEASUREMENTS AND CASE STUDY

A. Observational campaign

WRF-LES with the GAD is used to simulate one case study from the Turbine Wake and Inflow Characterization Study (TWICS-2011)^{16,17}. TWICS-2011 measured the inflow to and wake from

a 2.3-MW wind turbine with a hub height of $z_H = 80$ m and a rotor diameter of $D = 101$ m, located at the National Renewable Energy Laboratory's National Wind Technology Center (NWTC) near Boulder, Colorado, during the spring of 2011. This study used measurements from three instrument platforms, including an 80-m meteorological tower (M2) and two lidar systems, a commercially available vertically-profiling Windcube lidar (WC),^{48,49} and the research-grade High Resolution Doppler Lidar (HRDL),⁵⁰ designed and developed at the National Oceanic and Atmospheric Administration's Earth System Research Laboratory.

The NWTC frequently experiences downslope flows from the Rocky Mountains, which are often channeled through Eldorado Canyon, providing a consistent wind direction at the site.⁵¹ Such channeling enables instrumentation to be positioned such that it is often upstream of the test turbines, providing measurement of inflow conditions.

M2 and WC observations were used to specify the forcing conditions used for the simulations, whereas HRDL scans of the flow field surrounding the turbine were used to evaluate wake characteristics. M2 was located approximately 1.1 km to the west-northwest of the turbine and provided 10-min average temperature, T , at heights of 2 m, 50 m, and 80 m, and horizontal wind speed, U , and direction, λ , at heights of 2 m, 5 m, 10 m, 20 m, 50 m, and 80 m above the surface.⁵² WC was located approximately 310 m to the west-northwest of the turbine, and provided 10-min average U and λ at heights of 40 m, 50 m, 60 m, 80 m, 100 m, 120 m, 140 m, 160 m, 180 m, and 200 m above the surface. Data from the WC, by virtue of it being closer to the turbine, were used to specify the wind forcing, whereas M2 data were used to estimate stability. Positioned 880 m at a bearing of approximately 310° from the turbine, HRDL could best resolve winds blowing directly out of Eldorado Canyon. Aitken et al.¹⁷ include a map showing instrument layout at the site.

B. Case Study Description

To facilitate evaluation of the GAD, the dataset was queried for periods featuring nearly steady values of the wind speed, inflow direction, in near alignment with the HRDL, and conditions sustained for sufficient durations such that representative averages of fluctuating flow and wake characteristics could be obtained. The period best matching these criteria occurred on April 22 between approximately 13:00 and 17:00 MST. Figure 1 shows observed U (top), λ (upper middle), T (lower middle), and gradient Richardson number, Ri (bottom) values using data at 50 and 2 m, from this period. The period features nearly steady U , and λ values, with only gradual changes of T and Ri . Figure 1a shows negative shear values at the location of M2 but not at WC. This difference likely results from local terrain effects influencing the flow near M2.

The data depicted in Figure 1 are consistent with weak to moderately convective conditions, as indicated by the time series of T and Ri , as well as the ranges of U and λ values with height at different times. Decreasing T and Ri values indicate gradual weakening of convection with the reduction of insolation. Although trends are evident for T and Ri , the absence of corresponding trends in U and λ suggests relatively constant large-scale forcing, with the major source of variability being intermittent cloud cover, leading to changes in insolation, hence variations in the magnitudes of the surface sensible heat flux, H_S . Although H_S was not measured at the NWTC during TWICS-2011, due to its proximity to the complex and highly heterogeneous upstream conditions, and the relatively high sustained wind speeds observed during the period, it is unlikely that local heat flux values would have significantly altered turbulence and ABL structure. Given these uncertainties, values of 20 and 100 W m⁻² are specified for the simulations to represent the weakly and moderately convective conditions suggested by the measured data.

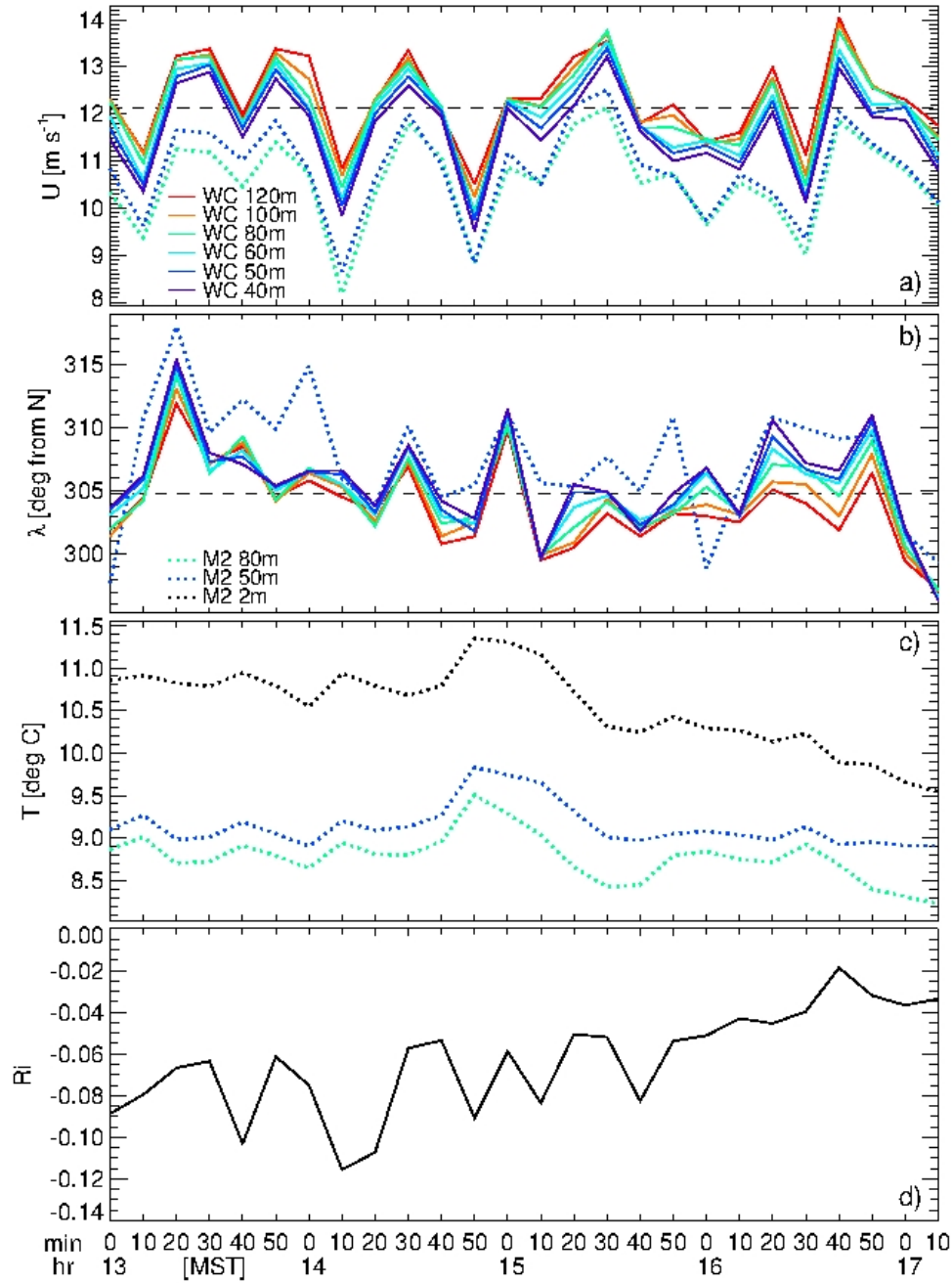


Figure 1. Ten-min average values of U (top), λ (upper middle), T (lower middle) and Ri (bottom), using data at 50 and 2 m, measured between 13:00 and 17:10 MST on April 22, 2011, at various heights from an instrumented tower (M2) and a vertically-profiling lidar (WC) upwind of the turbine. The horizontal dashed lines indicate mean values.

III. SIMULATION SETUP

The simulation framework utilized idealized LES consisting of two domains, with a fine-scale LES nested one-way within a coarser bounding LES. The coarser LES utilized periodic lateral boundary conditions and was run for several hours to develop turbulent flow consistent with the specified geostrophic wind and surface forcing. The coarse LES solution provided turbulent boundary conditions to the finer nested domain, within which the GAD was located and all analysis was performed. Table 1 provides a list of domain dimensions and parameter values.

TABLE I. Physical and computational dimensions of simulation domains, in which n_x , n_y , and n_z represent the number of grid points in the x , y , and z directions; Δx and Δz represent the horizontal and vertical grid spacings; and L_x , L_y , and L_z represent the domain dimensions. Δz is an approximate value for $z < 200$ m, above which it is stretched, as described in the text. The nested domain's lower left corner begins at $[i, j] = [65, 32]$ in the outer domain, where i and j indicate grid cell indices in the x and y directions, respectively.

	n_x	n_y	n_z	Δx [m]	Δz [m]	L_x [m]	L_y [m]	L_z [m]
Outer Domain	268	138	64	30	10	8010	4110	1700
Nested Domain	415	214		10		4140	2130	

The simulations use mesh resolutions of $\Delta x = \Delta y = 30$ m and 10 m on the outer and nested domains, respectively, and $\Delta z \cong 10$ m on both domains. WRF utilizes a pressure-based vertical coordinate given by $\eta = (p - p_t)/(p_s - p_t)$, where p_t and p_s are the pressure values at the model top and surface. Such a formulation precludes precise specification of Δz values. Initial Δz values were specified using the hypsometric equation, with $p_s = 1 \times 10^5$ Pa, temperatures

from the standard atmosphere, and constant values of $\Delta z = 10$ m up to a height of 200 m, above which Δz was stretched by 5% per grid level, up to a height of $z \cong 1700$ m. A Rayleigh damping layer with a coefficient of 0.003 s^{-1} was applied to the upper 700 m of each domain. WRF imposes vertical velocity $w = 0$ and stress $\tau_{ij} = 0$ at the model top. WRF's default fifth- and third-order horizontal and vertical advection schemes, respectively, were used.

The turbine hub was located at $[x_H, y_H] = [2070, 1070]$ m within the nested domain, providing streamwise distances of $20D$ and lateral distances of $10D$ in each direction, plus an additional 5 grid cells in each direction, over which the nested domain solutions is blended with that of the bounding domain. These distances provided substantial space for the inflow to develop smaller turbulence structures consistent with the finer mesh spacing on the nested domain, and also permitted sampling of the wakes to significant distances downstream.

Although other subgrid stress closures are available in WRF, the commonly-used Smagorinsky closure^{53,36} was chosen for this initial validation of the GAD. The WRF model's Smagorinsky closure is given by $\tau_{ij} = -2K_M \tilde{S}_{ij}$. Here, $K_M = (C_S l)^2 \max(0, |\tilde{S}_{ij}| - P_r^{-1} N^2)$ is the eddy viscosity coefficient for momentum, $C_S = 0.18$ is a constant, $l = (\Delta x \Delta y \Delta z)^{1/3}$ is a length scale (isotropic), $\tilde{S}_{ij} = \frac{1}{2} \left(\frac{\partial \tilde{u}_i}{\partial x_j} + \frac{\partial \tilde{u}_j}{\partial x_i} \right)$ is the resolved strain-rate tensor, $P_r^{-1} = 3$ is the inverse of the turbulent Prandtl number, and $N^2 = (g/\theta_0)/(\partial\theta/\partial z)$ is the Brunt-Väisälä frequency, where $g = 9.81 \text{ m s}^{-2}$ is the gravitational acceleration, $\theta = T(p_0/p)^{R/c_p}$ is the potential temperature, $R = 287 \text{ J kg}^{-1} \text{ K}^{-1}$ is the gas constant for dry air, $c_p = 1004 \text{ J kg}^{-1} \text{ K}^{-1}$ is the specific heat of dry air at constant pressure, and $\theta_0 = 290 \text{ K}$ is a reference value. Tildes denote the low-pass filtered, or resolved component of the flow, with $i = 1, 2, 3$ indicating the velocity components in the x -

(u), y- (v), and z- (w) directions, respectively. Scalar fluxes are given by $S_j = -2K_q \frac{\partial \tilde{q}}{\partial x_j}$, where K_q is the eddy viscosity coefficient for scalar q , given by $K_q = P_r^{-1} K_M$.

The surface boundary conditions were specified using the Monin-Obukhov similarity theory.⁵⁴ Surface stresses, τ_{i3}^s , $i = 1, 2$, where superscript s denotes surface values, are determined from $\tau_{i3}^s = -C_D U(z_1) u_i(z_1)$. Here, $U(z_1)$ and $u_i(z_1)$ are the resolved wind speed and horizontal velocity component, at their first computed heights above the surface, and $C_D = \kappa^2 \left[\ln \left(\frac{z_1 + z_0}{z_0} \right) - \psi_M \left(\frac{z_1}{L} \right) \right]^{-2}$ with $\kappa = 0.4$ the von Karman constant, z_1 the height corresponding to $U(z_1)$, and $z_0 = 0.1$ m the roughness length. For the convective conditions simulated herein, we follow Arya⁵⁵ and use $\psi_M \left(\frac{z}{L} \right) = \ln \left[\left(\frac{1 + \chi^2}{2} \right) \left(\frac{1 + \chi}{2} \right)^2 \right] - 2 \tan^{-1}(\chi) + \frac{\pi}{2}$, with $\chi = \left(1 - 15 \frac{z}{L} \right)^{1/4}$. Here, $L = [-u_*^3 \theta_{v0}] / [\kappa g (\overline{w \theta_v})_s]$ is the Obukhov length, where $\theta_v = \theta(1 + 0.61 q_v)$ is the virtual potential temperature, with q_v the water vapor mixing ratio, $\theta_{v0} = 290$ K, $u_* = [(\tau_{13}^s)^2 + (\tau_{23}^s)^2]^{1/4}$, and $(\overline{w \theta_v})_s = H_S / \rho C_p$ is the flux of θ_v at the surface. For the dry conditions simulated herein, $q_v = 0$, and $\theta_v = \theta$. Spatially and temporally uniform values of $H_S = 20$ and 100 W m^{-2} were specified to simulate weakly and moderately convective conditions.

The computational setup was simplified by applying a counterclockwise rotation of 35° , orienting the mean inflow angle approximately parallel to the x -axis, and permitting the GAD to be placed within the y - z plane, approximately perpendicular to the inflow. A geostrophic wind, V_g , of 14.5 m s^{-1} oriented from 292.5° (22.5° N of W) was specified for the LES, producing average values of U at z_H close to the 80-m WC value of 12.12 m s^{-1} averaged over the time period 13:00 to 17:10 MST on April 22, 2011, and $\lambda \cong 270^\circ$.

All simulations were initialized dry, and no cloud, radiation, land surface models or latent fluxes specified. Although intermittent cloudiness was observed during April 22, 2011, at the NWTC, for the idealized simulations conducted herein, the effects of radiation and its interactions with the cloud field and surface were captured by the two different values of H_S used to force the simulations. The simulations were initialized with uniform profiles of $\theta = 300$ K for $z < 500$ m, increasing by 10 K km^{-1} above, creating a capping inversion to prevent turbulence from reaching the model top, and initialized and forced with V_g and H_S as described above. Small perturbations, $\delta \in [\pm 0.25] \text{ K}$, obtained from a pseudo-random uniform distribution, were added to the initial values of θ as a decreasing cubic function of height up to 500 m.

Four hours of 1-min instantaneous velocity fields were generated using each of the two values of H_S . A spinup LES was run for 15 hours with $H_S = 20 \text{ W m}^{-2}$ to allow the solution to come into balance with V_g . The nested domain with the GAD was introduced at the beginning of hour 15. Data used for the analysis were collected beginning at hour 16 through hour 19. For the moderately-convective case, H_S was increased to 100 W m^{-2} at the beginning of hour 15.

IV. RESULTS

Figure 2 shows 10-min average (left) U and (right) λ profiles at z_H obtained from a square region containing 50 gridpoints in each horizontal direction about a point centered 600 m directly upstream of x_H , which sampled the inflow to the GAD. Each colored line depicts an average of 10 instantaneous profiles at 1-min intervals (proceeding temporally from dark blue, to light green), the thick black lines show averages over the entire four hours, the horizontal and vertical dashed lines correspond to z_H , and the average U from WC at z_H , and $\lambda = 270^\circ$. The top and bottom panels show profiles obtained from simulations using 20 and 100 W m^{-2} ,

respectively. The LES U values at 80 m span a similar range of values to those observed during the time period. The more strongly convective case shows reduced variability in U , but increased variability in λ , as a result of the existence of larger eddies that, although mixing momentum more uniformly, also more strongly influence the 10-min average values.

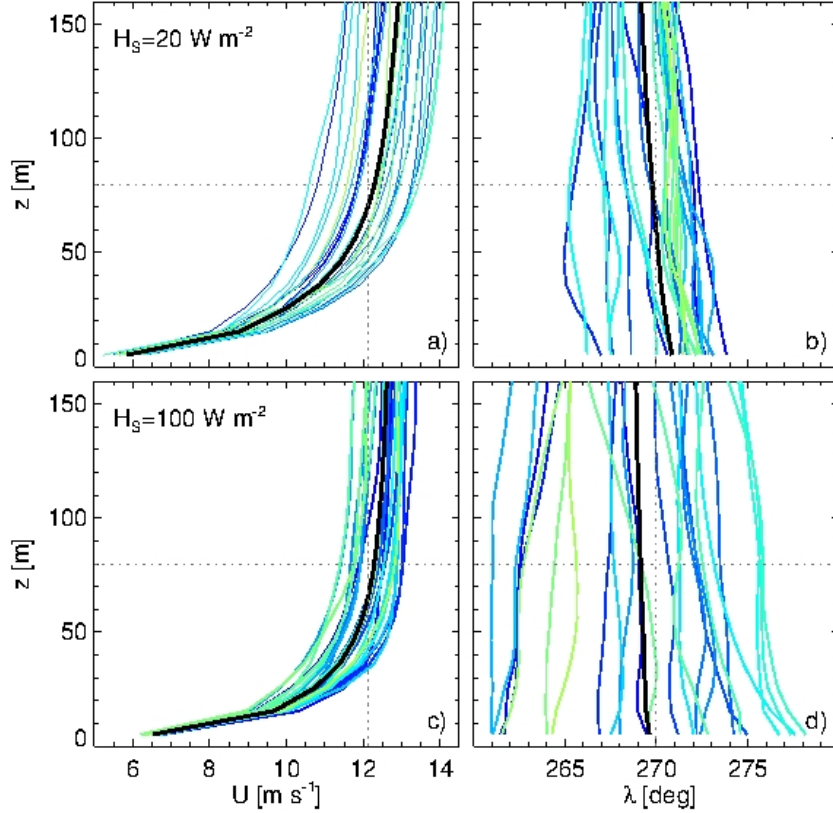


Figure 2. Ten-min average profiles (blue-green) of U (left) and λ (right) from LES using two H_g values, as indicated. The thin, horizontal, gray dotted lines indicate z_H , and the thin, vertical, gray dotted lines show the 80 m WC average value during the time period shown in Figure 1, and $\lambda = 270^\circ$, respectively. The thick black lines show the four-hour average LES values.

Two instantaneous contours of U at z_H , from the weakly (Figures 3a and 3b) and moderately (Figures 3c and 3d) convective simulations, indicate the spatial and temporal variability of both the flow field and wake characteristics. Although the wakes emanating from the GAD are clearly

discernible, their characteristics vary depending upon features of the background flow. Wakes appear to be shorter and less coherent during the moderately-convective conditions, as a result of the enhanced turbulent mixing and larger eddy sizes. In both cases, the wind speed deficits downstream from the GAD are comparable to the lowest wind speeds occurring within the background flow. The influence of the GAD can be better ascertained via time averaging of the flow field, which reduces much of the stochastic variability of the turbulent background flow.

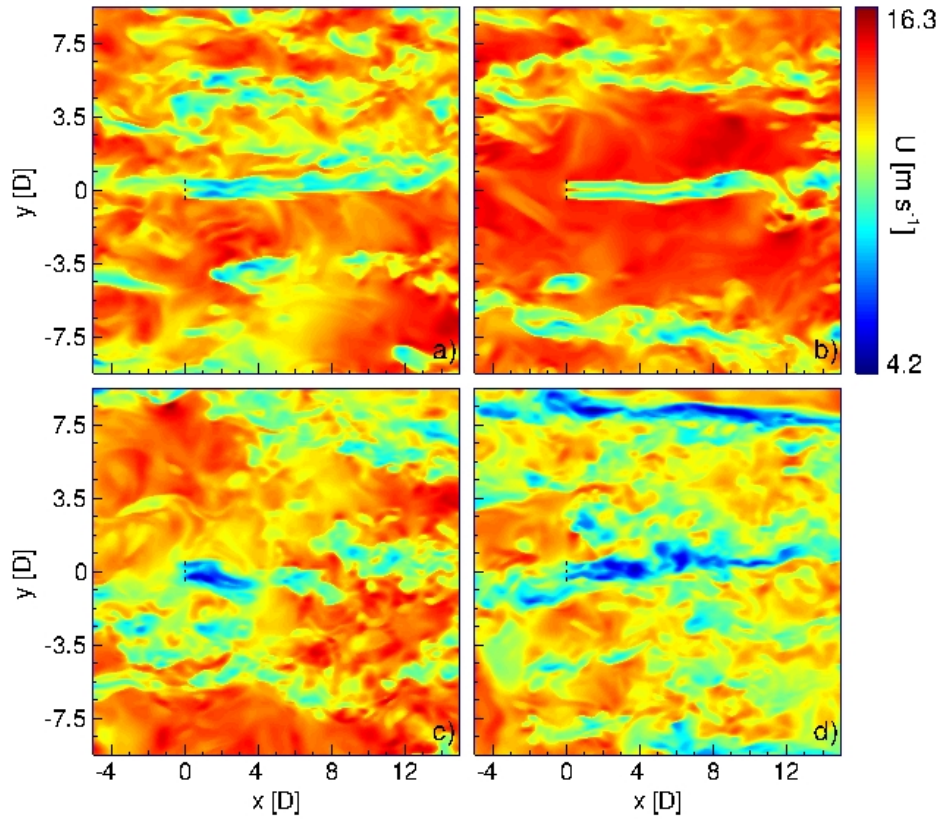


Figure 3. Instantaneous U values at z_H at the beginnings of (left) hours 17 and (right) 19, from the (top) weakly and (bottom) moderately convective simulations. The thin, vertical, black dotted line marks the position of the GAD at $x = y = 0D$.

Accordingly, Figure 4 shows four-hour average values of (left) u , (middle) v , and (right) w in the y - z plane, at the first gridpoint downstream from x_H , from the weakly convective case. The

central black dot indicates the GAD center, whereas the black dotted circle shows its perimeter. The gray dotted lines depict the locations of WRF's grid cell centers.

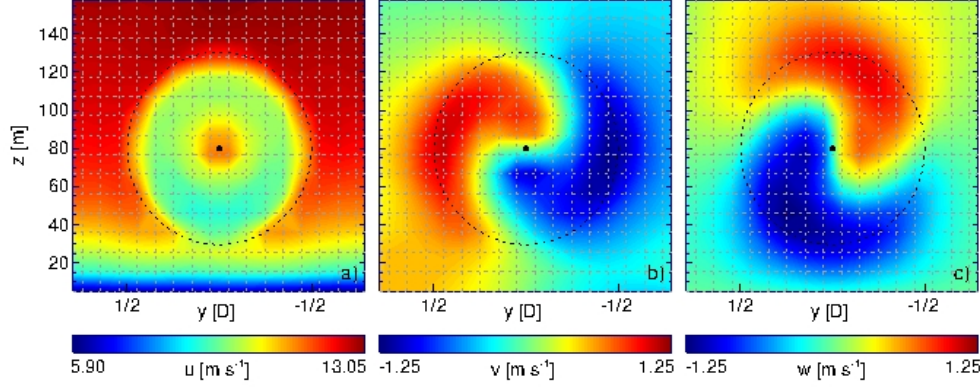


Figure 4. Four-hour averaged velocity components (left: u ; middle: v ; and right: w) at the location of the GAD in the y - z plane from the weakly convective case. The central black dot indicates the GAD center, whereas the black dotted circle shows its perimeter. The gray dotted lines depict the WRF model's grid cells.

The distributions are slightly asymmetric due to imperfect alignment of the flow in the normal direction, velocity shear in the vertical direction, and slight off-centering of the GAD in the vertical direction as a result of WRF's pressure-based vertical coordinate. Values of u show primarily the result of the turbine thrust, which exerts a drag force opposite the inflow direction. The v and w values show two effects: (1) flow divergence around the GAD, and (2) the torque imparted by the clockwise-rotating GAD, producing a counterclockwise rotation of the flow.

The wake effects decay in the streamwise and spanwise directions, as seen in the four-hour averaged u (Figures 5a and 5b) and w (Figure 5c) velocities in the x - y and x - z planes. The thin, black dotted lines depict the GAD location. The wakes again appear nearly, although not perfectly, symmetric about the center. Slightly lower minimum u -velocities are observed below and to the left of the GAD, with respect to the inflow direction. The lower velocities below arise

as a result of slower background mean velocities approaching the surface; those for $y < y_H$ arise because of the vertical velocities from the rotating wake transporting lower momentum air from below z_H upward, whereas those on the opposite side indicate downward transport of higher-momentum air from above z_H . The slightly larger magnitude of the negative w value for $y > y_H$ relative to the positive values on the opposite side reflects the slight misalignment of the mean inflow with the axial direction (see Figure 2b), resulting in some horizontal momentum being entrained into the rotating wake at $y > y_H$.

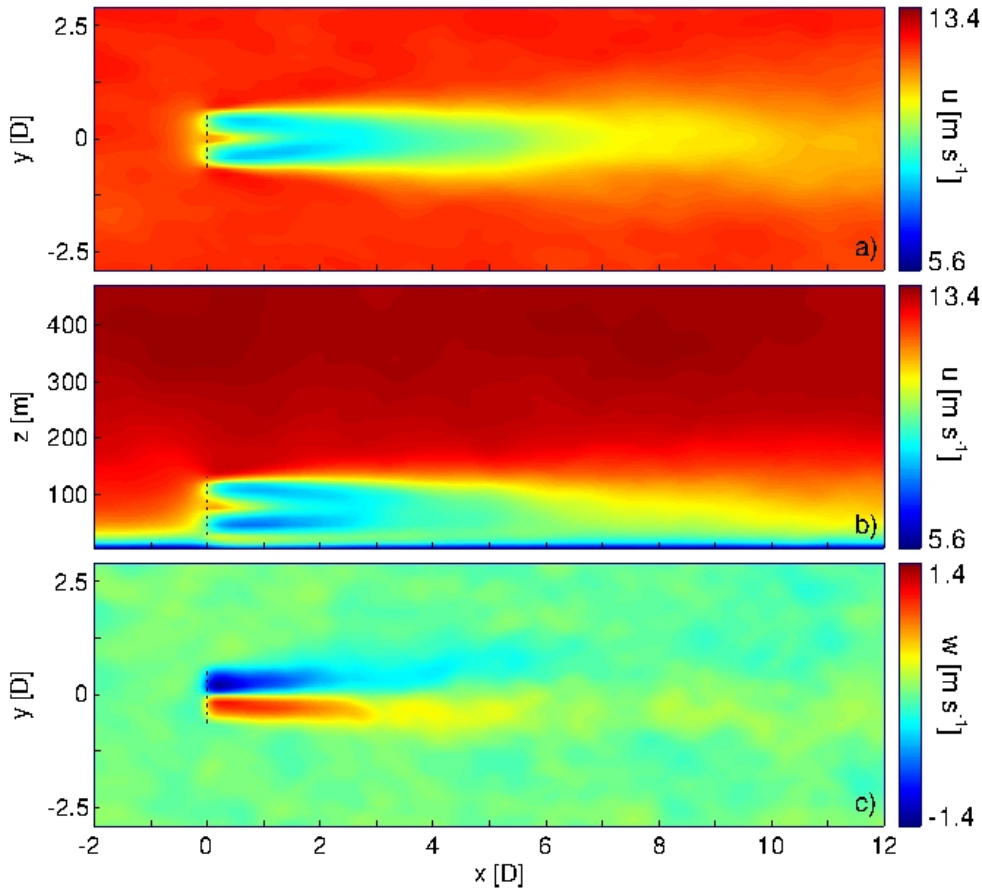


Figure 5. Four-hour averaged velocity components (top and middle: u ; bottom: w) at (top and bottom) z_H and (middle) y_H from the weakly convective simulation. The black dotted lines show the position of the GAD in the x - y and x - z planes.

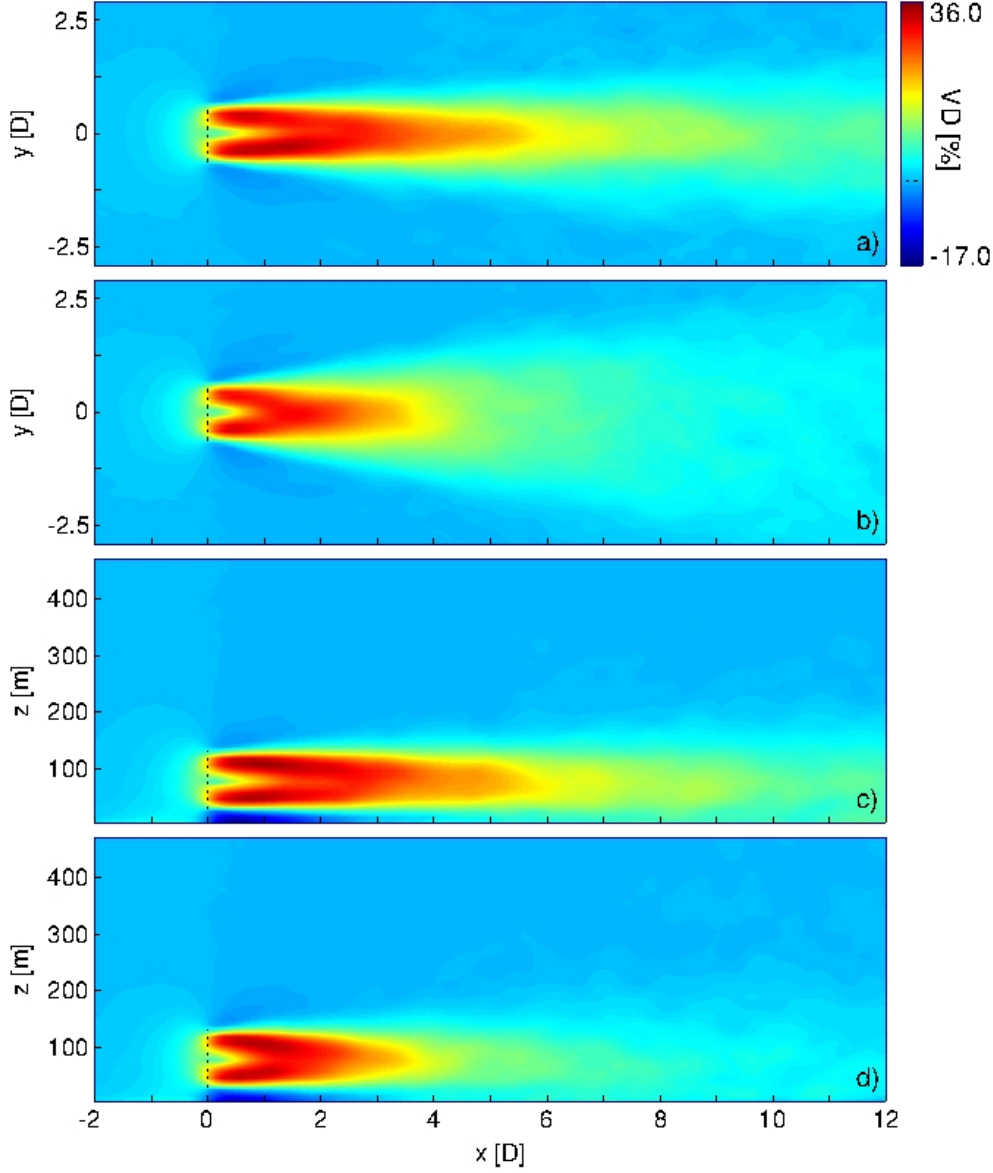


Figure 6. Four-hour averaged velocity deficits (VD) in the (upper) x - y and (lower) x - z planes, at z_H and y_H , respectively. The black dotted lines in the panels show the position of the GAD, whereas that in the color bar indicates the zero level. Results from both the weakly (Figures 6a and 6c) and moderately (Figures 6b and 6d) convective simulations are shown.

The velocity deficits (VD) imparted by the GAD onto the flow speed are shown in Figure 6. These values are computed from $VD = 100(U_{LES} - U_{GAD})/U_{LES}$, where U_{LES} and U_{GAD} are four-hour-averaged U values computed from the same LES setup, with one LES using the GAD and

one without. The top two panels of Figure 6 show x - y sections at z_H , whereas the bottom two panels show x - z sections at y_H . Results from both the weakly (Figs. 6ac) and moderately (Figs. 6bd) convective simulation are shown. Dotted lines in the panels indicate the GAD location, whereas the dotted line in the color bar indicates the zero level.

The simulated wake characteristics are influenced by the different values of H_5 . Although the peak magnitudes of the wake deficits from the weakly and moderately convective simulations are similar, noticeable differences emerge in their spatial extents, with the moderately convective case producing more-rapid lateral spreading and streamwise attenuation, likely caused by enhanced mixing. Although the primary effect of the GAD is to retard the downstream flow, slight increases are observed around the perimeter of the GAD, consistent with observations from Bingöl et al.⁵⁶ The larger increases observed beneath the rotor are hypothesized to be caused by (1) flow being deflected around the perimeter of the disk via pressure effects, thereby squeezing between the disk and the surface (as in Rajewski et al.²³) and (2) the relatively lower ambient wind speeds near the surface, magnifying the percent change.

V. WAKE COMPARISON WITH OBSERVATIONS

HRDL operated continuously from 13:00 to 17:00 MST on April 22, cycling through several scanning modes, as described by Smalikho et al.¹⁶ and Aitken et al.¹⁷ HRDL data are used to estimate the wake velocity deficit, enabling comparison of results from the LES with the GAD. Briefly, at each range gate within each scan, a parameterized statistical model (Aster et al.⁶⁰) is fit to the measured horizontal wind speed profile. The ambient wind field is modeled as having uniform speed and direction, while the wake is modeled as a Gaussian function subtracted from this uniform background flow. Various wake characteristics, such as the velocity deficit, are

determined from parameters in the statistical model, whose best-fit values are obtained using weighted nonlinear regression, in which observation weights are specified using the Cramer-Rao lower bound (Rye and Hardesty⁶¹). Further details may be found in Aitken et al.¹⁷.

Figure 7 shows horizontal plan-position indicator (PPI) scans of radial velocity obtained at an elevation angle of 2° , which intersected the turbine near z_H , the location of which is shown by the white lines. Each PPI scan lasted approximately 20 seconds, providing a quasi-instantaneous snapshot of the flow field. PPI scans taken at four different times are shown, with two occurring during the weakly convective latter stages of the period (Figures 7a and 7b), and two from earlier, when the mean convection was stronger (Figures 7c and 7d). As with the snapshots from the LES shown in Figure 2, the nearly instantaneous wakes observed by HRDL show significant spatial and temporal variability during the periods depicted in Figure 7, with magnitudes similar to the variability of the background flow.

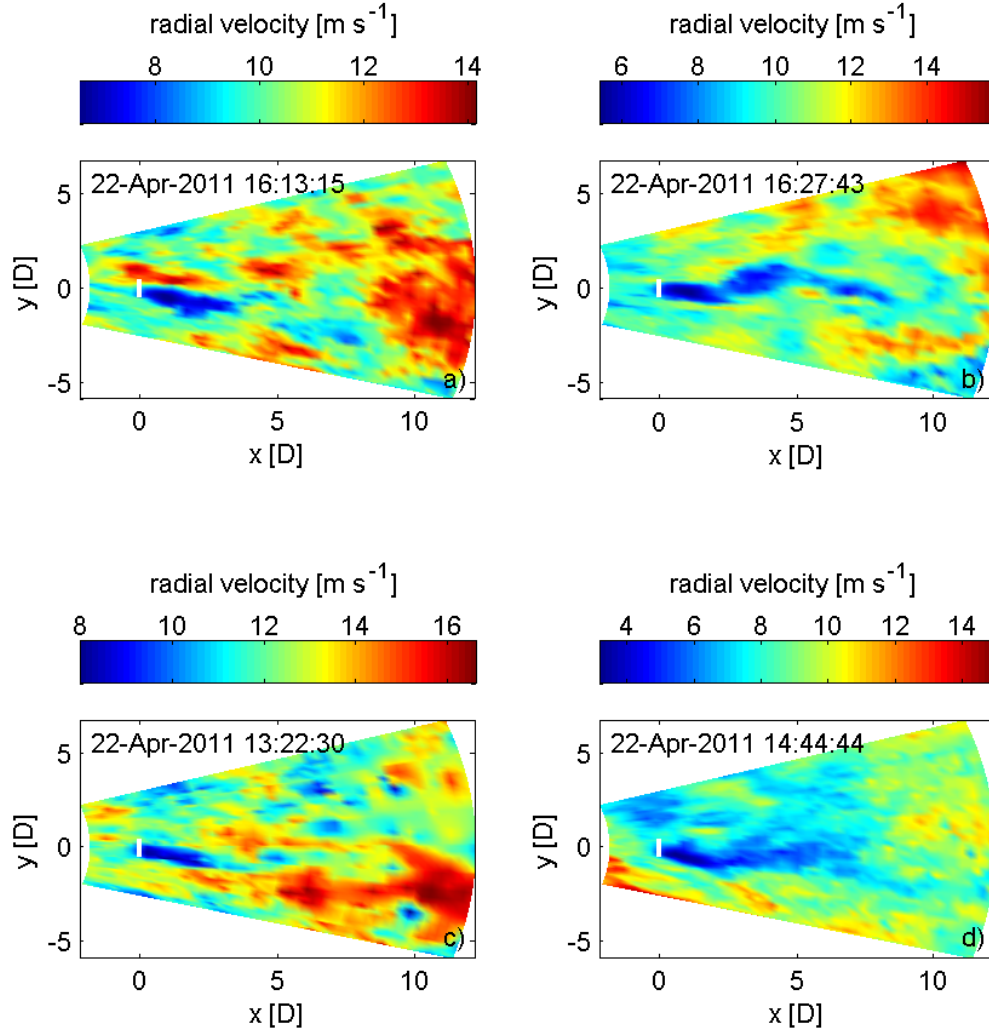


Figure 7. HRDL PPI scans of radial velocity using an elevation angle of 2° . White lines show the turbine location. Four scans are shown, two each occurring during the weakly convective (a and b) and moderately convective (c and d) portions of the time period shown in Figure 1. HRDL's beam intersects the turbine approximately 45 m above the ground, and increases by about 35 m at $x = 10D$.

VD values calculated from the HRDL data (as outlined in Aitken et al.¹⁷) are shown in Figure 8, which depicts the distribution of VD as a function of downwind distance from all PPI scans occurring between 13:00 and 17:10 MST on April 22, 2011. The black central line depicts the median value, whereas the shaded region indicates one standard deviation on either side. VD

values from the LES computed using the same algorithm as applied to the observations are also shown, with the blue and red lines indicating the average values from the weakly and moderately convective LES, respectively.

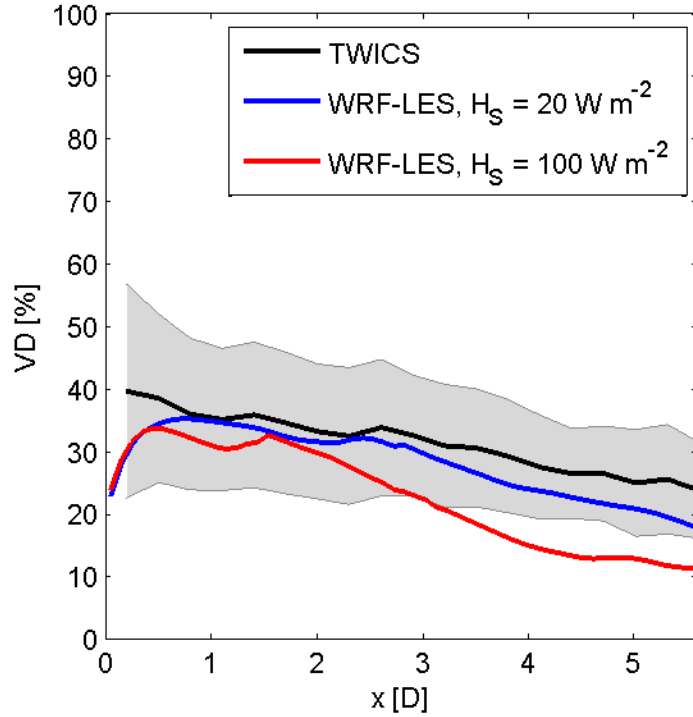


Figure 8. Velocity deficit (VD) as a function of downstream distance occurring between 13:00 and 17:10 MST on April 22, 2011. The black, bold, central line indicates median observed values, whereas the symmetric shaded error bars represent the standard deviation of the measurements. Mean VD values from the LES of weakly and moderately convective conditions are shown by the blue and red lines, respectively.

The overall agreement between the LES and the observations is good, especially for the weakly convective conditions, with the simulations underpredicting VD values slightly, and producing somewhat more rapid attenuation. The moderately convective simulations also produce good

agreement for downstream distances less than approximately $2D$, before attenuating much more rapidly than the observations.

Because of the absence of direct measurements of H_S , no straightforward method could be found to clearly separate the observations into weakly and moderately convective periods. The closer agreement between the weakly convective LES and the observed VD values suggests predominantly weak convection occurring during the time period. However, errors caused by both the limitations of the GAD model and the idealized setup must be acknowledged.

VI. SUMMARY AND CONCLUSIONS

A generalized actuator disk (GAD) wind turbine wake model was implemented into the Weather Research and Forecasting (WRF) model for large-eddy simulation (LES) applications. A fine LES with the GAD model was nested within a coarser-bounding LES, which provided turbulent inflow and boundary conditions. Idealized simulations were carried out using flat terrain and uniform forcing approximating weakly and moderately convective conditions. Simulation results were evaluated for physical consistency and compared with observations obtained from high-resolution Doppler lidar (HRDL) scans taken in the presence of an operating wind turbine during the TWICS-2011 field experiment at the National Renewable Energy Laboratory's National Wind Technology Center near Boulder, Colorado. The LES with the GAD produced results that were physically consistent with expected wake behavior, including reasonable rates of rotation and flow reduction. Velocity deficits (VD) computed from the weakly-convective LES agreed quite well with those obtained from the observations, with the LES producing slightly smaller magnitudes and more-rapid attenuation. The moderately convective LES produced similar VD values very close to the GAD, but featured much more-rapid attenuation with downstream

distance. Further investigations will be required to evaluate the changes of simulated wake characteristics under different stability conditions.

As with most computational investigations of real-world phenomena, several potential sources of error were present in this study. The idealization of the LES setup ignored nontrivial sources of variability, chief among these the very complex inflow, which emanates from the Rocky Mountains to the west, is channeled through Eldorado Canyon, exits a dense forest canopy, and encounters rolling shrubland and grassy terrain during its transit to the NWTC. Given the complexity of the inflow, locally measured surface parameters (i.e., heat flux, roughness length) may be of questionable applicability to idealized LES.

Beyond the inherent limitations of the GAD model itself, other sources of error include the use of imperfect turbine aerodynamic and operational parameters, which were provided as approximations to those of the test turbine used during the observational campaign. The relatively coarse mesh resolution employed during this study likewise precluded representation of drag from the hub and tower. Use of the Smagorinsky turbulence closure, which has been shown to be more strongly dissipative of smaller scales than other approaches,^{30,31,47} may also have inhibited formation of structures containing low velocities in the wakes. In addition, the average LES wind speeds were slightly over predicted relative to the observations, by 1.38 % and 1.34 %, during the weakly and moderately convective simulations, respectively. While these differences are quite small, as wake effects typically peak at wind speeds below rated power and lessen as speeds increase through Region III of the power curve,⁵⁷ a slightly lower wind speed would show slightly larger VD values, further improving agreement with the observed values.

Nevertheless, this study demonstrates the efficacy and promise of a methodology of using WRF-LES with GAD wind turbine wake models for conducting detailed simulations of wake effects and wake/turbulence interactions under increasingly realistic atmospheric forcing scenarios. Implementation of the GAD into the WRF model provides a flexibility to address the shortcomings of idealized setups by incorporating more sophisticated inflow from mesoscale simulations, permitting representation of important sources of variability imposed by the complexity of the upstream environment. Future investigations using increasingly realistic setups will enable further refinement of the GAD model and WRF-LES-GAD approach.

ACKNOWLEDGEMENTS

We thank the following for their helpful contributions: Nikola Marjanovic, Matthew Churchfield, Bob Banta, Yelena Pichugina, Neil Kelley, Alan Brewer, and the turbine manufacturer. This work was performed under the auspices of the U.S. Department of Energy by Lawrence Livermore National Laboratory under contract DE-AC52-07NA27344, and was supported by the U.S. Department of Energy under Contract No. DE-AC36-08-GO28308 with the National Renewable Energy Laboratory. LLNL-JRNL-639893.

APPENDIX

Although further details of the Blade Element Momentum theory and the GAD can be found in the references, a brief background and details of implementation of the GAD into WRF are provided here. The GAD computes lift and drag forces using aerodynamic properties of the turbine blades and the inflow velocity at the rotor plane. Induction factors are employed to incorporate modifications to the flow field near the blades because of interactions with the blades and wake. The induction factors are obtained by equating expressions for increments of thrust, dT , and torque, dM , obtained two different ways, one from consideration of the stream tubes intersecting the turbine and another from blade aerodynamics.

1. Stream Tube Dynamics

The mass flow rate within a stream tube intersecting the disk containing the rotating turbine is a constant, given by $\dot{m} = \rho V \pi r^2$, where ρ is the fluid density, V is the wind speed in the direction normal to the disk, and r is the stream tube radius. An expression for dT can be obtained by considering the difference between the free-stream upwind velocity V_0 , and a reduced V_2 at a location downstream from the turbine, as shown in Figure A1. Assuming that the turbine thrust is the only agent responsible for this decrease yields $dT = (V_0 - V_2)d\dot{m}$, where

$$d\dot{m} = 2\pi r \rho V_1 dr \tag{A1}$$

is the incremental change in mass flow rate per radial increment dr , and V_1 is the stream tube velocity at the disk location.

The velocity normal to the disk, V_1 , is reduced from its upstream value as a result of the widening of the stream tube. This effect is accounted for via the normal induction factor a_n , giving

$$V_1 = V_0(1 - a_n). \quad (\text{A2})$$

A similar expression can be derived for the downstream velocity by equating the flow speed reduction with the pressure drop at the disk, found by applying Bernoulli's equation,⁵⁸ which gives

$$V_2 = V_0(1 - 2a_n). \quad (\text{A3})$$

Equations A1 through A3 can be combined to yield an equation for the incremental change in thrust,

$$dT = 4\rho\pi r a_n(1 - a_n)V_0^2 dr. \quad (\text{A4})$$

A similar expression for dM can be obtained by taking the time rate of change of the angular momentum, $I\omega$, for a stream tube rotating at angular velocity ω with moment of inertia $I = mr^2$, giving $M = \dot{m}r^2\omega$. Combining this result with Equations A1 and A2 yields

$$dM = 2\pi r^3 \rho V_0(1 - a_n)\omega dr. \quad (\text{A5})$$

Equation A5 can be cast in terms of the turbine's rotational velocity, Ω , which induces a tangential velocity of

$$V_t = \Omega(1 + a_t)r. \quad (\text{A6})$$

Here, the tangential induction factor, a_t , accounts for rotation of the stream tube in the direction opposite that of the turbine. Positing that ω takes half of its downstream value at the location of the rotor disk⁵⁹ yields $a_t = \omega/2\Omega$. Using this result with Equations A5 and A6 gives

$$dM = 4\pi r^3 \rho V_0 (1 - a_n) a_t \Omega dr. \quad (\text{A7})$$

2. Blade Aerodynamics

The incremental thrust and torque produced by a small annular element of the disk can be expressed as

$$dT = B F_n dr \quad (\text{A8})$$

and

$$dM = B F_t r dr, \quad (\text{A9})$$

where B is the number of blades and F_n and F_t are the normal and tangential forces, per unit

length, obtained from $\begin{bmatrix} F_n \\ F_t \end{bmatrix} = \begin{bmatrix} \cos \psi & \sin \psi \\ \sin \psi & -\cos \psi \end{bmatrix} \begin{bmatrix} L \\ D \end{bmatrix}.$ (A10)

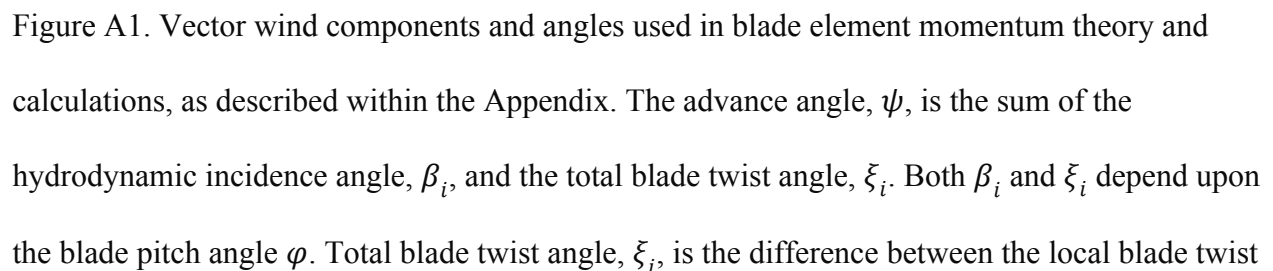
Here, ψ is the advance angle of the blade with respect to the plane of rotation (see Figure A1),

and L and D are the lift and drag forces on the blade, per unit length, given by

$$L = \frac{1}{2} \rho V_r^2 c C_l \quad (\text{A11})$$

and

$$D = \frac{1}{2} \rho V_r^2 c C_d, \quad (\text{A12})$$

$$dT = \frac{1}{2} \rho V_r^2 B c C_n dr \quad (\text{A13})$$
$$dM = \frac{1}{2} \rho V_r^2 B c C_t r dr, \quad (\text{A14})$$
$$\begin{bmatrix} C_n \\ C_t \end{bmatrix} = \begin{bmatrix} \cos \psi & \sin \psi \\ \sin \psi & -\cos \psi \end{bmatrix} \begin{bmatrix} C_l \\ C_d \end{bmatrix}. \quad (\text{A15})$$


angle and the blade pitch angle, φ . In our implementation of the GAD the blade pitch angle is a function of the wind speed, V_1 .

Obtaining expressions for the induction factors requires expressing V_r in Equations A13 and A14 in terms of the normal and tangential velocity components given by Equations A2 and A6.

Geometrical considerations (see Figure A1) give

$$V_0(1 - a_n) = V_r \sin \psi \quad (\text{A16})$$

and

$$\Omega r(1 + a_t) = V_r \cos \psi. \quad (\text{A17})$$

Substitution of Equation A15 into Equation A13 yields $dT = \frac{1}{2} \rho [V_0^2(1 - a_n)^2 / \sin^2 \psi] B c C_a dr$

which, if equated with Equation A4, yields

$$a_n = \left[1 + \frac{4 F \sin^2 \psi}{s C_n} \right]^{-1}. \quad (\text{A18})$$

Here, the solidity factor $s = \frac{cB}{2\pi r}$, which accounts for the density of blades, has been used, and

$F = F_{tip} + F_{hub} = \frac{2}{\pi} \cos^{-1}(\exp[-f_{tip}]) + \frac{2}{\pi} \cos^{-1}(\exp[-f_{hub}])$ accounts for vorticity

generation at the blade tips and hub, with $f_{tip} = B(r_{tip} - r)/(2r \sin \psi)$, and

$f_{hub} = B(r - r_{hub})/(2r \sin \psi)$. Here r_{tip} and r_{hub} are the radii of the disk and hub.

An expression for a_t can be similarly obtained using Equations A14 through A16, yielding

$dM = \frac{1}{2} \rho [V_0(1 - a_n)\Omega(1 + a_t)/(\sin \psi \cos \psi)] B c C_n dr$, which, if equated with Equation A7,

and incorporating s and F , gives

$$a_t = \left[\frac{4 F \sin \psi \cos \psi}{s C_t} - 1 \right]^{-1}. \quad (\text{A19})$$

The induction factors a_n and a_t account for modifications of V_0 , an unperturbed upstream value, as the flow approaches the disk. However, LES with the GAD explicitly resolves a reduction of the normal flow component approaching the disk plane (see Figures 4 through 6). The velocity computed at the turbine rotor location is therefore V_1 , and it is not necessary to explicitly compute the normal induction factor. Because the reduction of V_0 approaching the GAD is resolved, only the component of a_n related to tip and hub losses, which are not resolved, must be computed. Herein, we use a value of $a_n = 0.02$, which is nearly constant across the power curve, obtained as the difference between computing a_n using Equation A18 with and without F . The tangential induction factor is computed using Eq. A19, because the effects accounted for by a_t are not explicitly resolved.

3. Solution Procedure

Because the value of a_t depends upon the lift and drag forces, which in turn depend on a_t , we employ an iterative solution procedure using the following steps:

1. Assume an initial value for a_t .
2. Obtain V_1 at the GAD location.
3. Calculate V_t from Equation A6.
4. Calculate the blade pitch angle, φ , as a function of V_1 .
5. Calculate the twist angle, ξ , as a function of radial distance from the hub center.

6. Calculate $\beta = \psi - \xi + \varphi$, where $\psi = \tan^{-1}(V_1/V_t)$.

7. Calculate C_l and C_d as functions of β .

8. Calculate C_t and C_n from Equation A15.

9. Calculate a_t from Equation A19.

Steps 4 through 7 require information specific to the turbine and its operation. The values used herein were provided by the manufacturer as an approximation to those of the 2.3-MW turbine at the NWTC. Steps 2 through 9 are repeated until the current iteration changes a_t by less than a threshold value of 1×10^{-5} . Thereafter, the blade element lift and drag forces are computed from Equations A11 and A12, and projected onto the normal and tangential directions, with respect to the GAD, using Equation (A10). F_n and F_t are then projected onto WRF's $[x, y, z]$ coordinates as

$$F_x = F_n \cos \Phi + F_t \sin \zeta \sin \Phi \quad (\text{A20})$$

$$F_y = F_n \sin \Phi - F_t \sin \zeta \cos \Phi \quad (\text{A21})$$

$$F_z = -F_t \cos \zeta, \quad (\text{A22})$$

where Φ and ζ describe the orientation of a point P on the actuator disk with respect to WRF's $[x, y, z]$ coordinate system, as shown in Figure A2.

F_x , F_y and F_z are added to WRF's momentum equations as

$$\frac{\partial u}{\partial t} = -\frac{1}{2\pi r \rho} G(d_n) F_x \quad (\text{A23})$$

$$\frac{\partial v}{\partial t} = -\frac{1}{2\pi r \rho} G(d_n) F_y \quad (\text{A24})$$

$$\frac{\partial w}{\partial t} = -\frac{1}{2\pi r \rho} G(d_n) F_z. \quad (\text{A25})$$

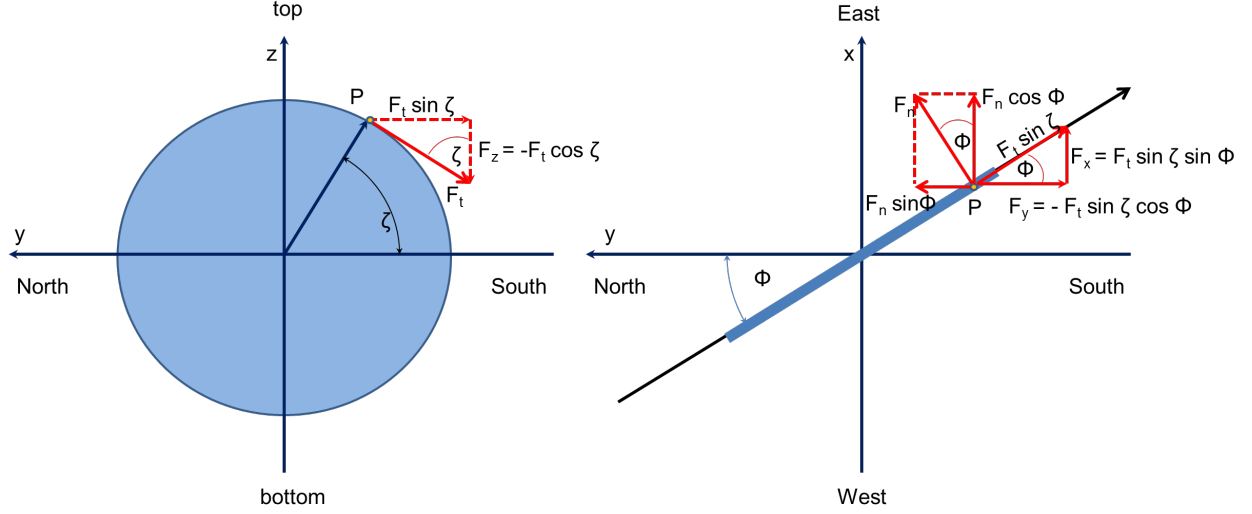


Figure A2. Projection of axial and tangential blade forces F_n and F_t , onto WRF's $[x, y, z]$ coordinate system.

Here, the factor of $2\pi r$ is the circumference of the annular element at a distance r from the hub center, and $G(d_n) = \frac{1}{\sigma\sqrt{2\pi}} \exp\left[-\frac{d_n^2}{2\sigma^2}\right]$ applies the forces computed within the plane of the disk over several computational gridpoints in the normal direction, to avoid numerical instabilities that can arise when strong forces are applied at isolated grid points. $G(d_n)$ is centered about the disk plane, with a width controlled by the standard deviation σ , herein set to Δx .

The present implementation of the GAD does not include a source term for subgrid TKE, as LES with sufficient mesh resolution to resolve the GAD should also resolve most of the TKE, with the subgrid component playing a minor role. Inclusion of a subgrid TKE production model is compatible with the existing framework.

REFERENCES

- ¹M. Magnusson, and A. S. Smedman, “Influence of atmospheric stability on wind turbine wakes,” *Wind Eng.* **18**, 139–151 (1994).
- ²R. J. Barthelmie, S. C. Pryor, S. T. Frandsen, K. S. Hansen, J. G. Schepers, K. Rados, W. Schlez, A. Neubert, L. E. Jensen, and S. Neckelmann, “Quantifying the Impact of Wind Turbine Wakes on Power Output at Offshore Wind Farms,” *J. Atmos. Ocean. Tech.* **27**(8), 1302–1317 (2010).
- ³S. Wharton, and J. K. Lundquist, “Atmospheric Stability Impacts on Power Curves of Wind Turbines: An Analysis of a West Coast North American Wind Farm,” *Environ. Res. Lett.* **7** 014005 (2012).
- ⁴N. D. Kelley, “An initial overview of turbulence conditions seen at higher elevations over the Western Great Plains,” *Global Windpower 2004 Conference proceedings* (Chicago, 2004).
- ⁵N. Kelley, M. Shirazi, D. Jager, S. Wilde, J. Adams, M. Buhl, P. Sullivan, and E. Patton, “Lamar Low-Level Jet Program – Interim Report,” Report No. NREL/TP-500-34593, National Renewable Energy Laboratory, Golden, CO, 2004.
- ⁶C. Sim, S. Basu, and L. Manuel, “The influence of stable boundary layer flows on wind turbine fatigue loads,” *Proceedings of the Aerospace Sciences Meeting AIAA*, (Orlando, 2009).
- ⁷W. J. Shaw, J. K. Lundquist, and S. J. Schreck, “Workshop on Research Needs for Wind Resource Characterization,” *Bull. Amer. Meteor. Soc.* **90**, 535–538 (2009).

⁸B. Sanderse, S. P. van der Pijl and B. Koren, “Review of computational fluid dynamics for wind turbine wake aerodynamics,” *Wind Energy* 14, 799–819 (2011).

⁹F. J. Zajackowski, S.E. Haupt, and K.J. Schmehl, “A preliminary study of assimilating numerical weather prediction data into computational fluid dynamics models for wind prediction,” *J. Wind Eng. Ind. Aerodyn.* **99**, 320–329 (2011).

¹⁰R. B. Stull, *An Introduction to Boundary Layer Meteorology*, (Kluwer Academic Publisher, Dordrecht, 1988).

¹¹W. Blumen, R. M. Banta, S. P. Burns, D. C. Fritts, R. Newsom, G. S. Poulos, and J. Sun, “Turbulence statistics of a Kelvin–Helmholtz billow event observed in the night-time boundary layer during the Cooperative Atmosphere–Surface Exchange Study field program,” *Dynamics of Atmospheres and Oceans* **34**(2–4), 189–204 (2001).

¹²J. Sun and coauthors, “Atmospheric disturbances that generate intermittent turbulence in nocturnal boundary layers,” *Boundary-Layer Meteorol.*, **110**, 255–279 (2004).

¹³N. D. Kelley, B. J. Jonkman, G. N. Scott, J. T. Bialasiewicz, and L. S. Redmond, “The impact of coherent turbulence on wind turbine aeroelastic response and its simulation,” *Wind Power 2005 Conference Proceedings* (Denver, 2005).

¹⁴U. Högström, D. N. Asimakopoulos, H. Kambezidis, C.G. Helmis, and A. Smedman, “A field study of the wake behind a 2 MW wind turbine,” *Atmos. Environ.* **22**, 803–820 (1988).

¹⁵M. Magnusson, and A.-S. Smedman, “Air flow behind wind turbines,” *J. Wind Eng. Ind. Aerodyn.* **80**, 169–189 (1999).

- ¹⁶I. N. Smalikho, V. A. Banakh, Y. L. Pichugina, W. A. Brewer, R. M. Banta, J. K. Lundquist, and N. D. Kelley, “Lidar investigation of atmosphere effect on a wind turbine wake,” *Accepted for publication in J. Atmos. Ocean. Tech.* (2013).
- ¹⁷M. L. Aitken, R. M. Banta, Y. L. Pichugina, and J. K. Lundquist, “Quantifying wind turbine wake characteristics from scanning remote sensor data,” *In review at J. Atmos. Ocean. Tech.* (2013).
- ¹⁸M. J. Churchfield, S. Lee, J. Michalakes, and P. J. Moriarty, “A numerical study of the effects of atmospheric and wake turbulence on wind turbine dynamics,” *J. Turbulence* **13**(14), 1–32 (2012).
- ¹⁹J. Meyers, and C. Meneveau, “Optimal turbine spacing in fully developed wind farm boundary layers,” *Wind Energy* **15**, 305–317 (2012).
- ²⁰D. L. Elliott, and J. C. Barnard, “Observations of wind turbine wakes and surface roughness effects on wind flow variability,” *Sol. Energy* **45**, 265–283 (1990).
- ²¹D. Kaffine, and C. Worley, “The Windy Commons?,” *Environmental and Resource Economics* **47**(2) 151–172 (2010).
- ²²S. Baidya Roy, “Simulating impacts of wind farms on local hydrometeorology,” *J. Wind Eng. Indust. Aerodyn.* **99**, 491–498 (2011).
- ²³D. Rajewski, E.S. Takle, J. K. Lundquist, M. E. Rhodes, S. Oncley, and T. Horst, “The CWEX Experiments,” *Accepted for publication in Bull. Amer. Meteorol. Soc.* (2013)

- ²⁴M. J. Churchfield, S. Lee, P. J. Moriarty, L. A. Martínez, S. Leonardi G. Vijayakumar, and J. G. Brasseur, “A large-eddy simulation of wind-plant aerodynamics,” *Proceedings of the Aerospace Sciences Meeting AIAA* (Nashville, 2012).
- ²⁵S. Lee, M. Churchfield, P. Moriarty, J. Jonkman, and J. Michalakes, “Atmospheric and wake turbulence impacts on wind turbine fatigue loading, *Proceedings of the Aerospace Sciences Meeting AIAA* (Nashville, 2012).
- ²⁶P. P. Fleming, J.-W. Gebrad, S. Wingerden, S. Lee, M. Churchfield, A. Scholbrock, J. Michalakes, K. Johnson, and P. Moriarty, “The SOWFA super-controller: A high fidelity tool for evaluating wind plant control approaches,” *Proceedings of the European Wind Energy Association* (Vienna, 2013).
- ²⁷W. C. Skamarock, and Coauthors, “A description of the advanced research WRF version 3,” Report No. NCAR/TN-4751STR, National Center for Atmospheric Research, Boulder, CO, 2008
- ²⁸C.-H. Moeng, J. Dudhia, J. B. Klemp, and P. P. Sullivan, “Examining two-way nesting for large eddy simulation of the PBL using the WRF model,” *Mon. Wea. Rev.* **135**, 2295–2311 (2007).
- ²⁹J. D. Mirocha, J. K. Lundquist and B. Kosović, “Implementation of a nonlinear subfilter turbulence stress model for large-eddy simulation in the Advanced Research WRF model,” *Mon. Wea. Rev.* **138**, 4212–4228 (2010).
- ³⁰J. D. Mirocha, G. Kiril, E. Bou-Zeid, F. K. Chow, and B. Kosović, “Transition and equilibration of neutral atmospheric boundary layer flow in one-way nested large eddy

simulations using the Weather Research and Forecasting model,” *Mon. Wea. Rev.* **141**, 918–940 (2013).

³¹G. Kirkil, J. D. Mirocha, F. K. Chow, and E. Bou-Zeid, “Implementation and evaluation of dynamic subfilter-scale stress models for large-eddy simulation using WRF,” *Mon. Wea. Rev.* **140**, 266–284 (2012).

³²K. A. Lundquist, F. K. Chow, and J. K. Lundquist. “An immersed boundary method for the Weather Research and Forecasting model,” *Mon. Wea. Rev.* **138**, 796–817 (2010).

³³K. A. Lundquist, F. K. Chow, and J. K. Lundquist, “An Immersed Boundary Method Enabling Large-Eddy Simulations of Urban Terrain in the WRF model,” *Mon. Wea. Rev.* **140**, 3936–3955 (2012).

³⁴A. C. Fitch, J. B. Olson, J. K. Lundquist, J. Dudhia, A. K. Gupta, J. Michalakes, and I. Barstad, “Local and Mesoscale Impacts of Wind Farms as Parameterized in a Mesoscale NWP Model,” *Mon. Wea. Rev.* **140**(9), 3017–3038 (2012).

³⁵A. Fitch, J. K. Lundquist, and J. B. Olson, “Mesoscale influences of wind farms throughout a diurnal cycle,” *Mon. Wea. Rev.* **141**, 2173–2198 (2013).

³⁶D. K. Lilly, “The representation of small-scale turbulence in numerical experiment,” *Proceedings of the IBM Scientific Computing Symposium on Environmental Sciences* (New York, 1967) pp. 195–210.

³⁷J. W. Deardorff, “A numerical study of three-dimensional turbulent channel flow at large Reynolds numbers,” *J. Fluid Mech.* **41**, 453–480 (1970).

- ³⁸J. W. Deardorff, “Three dimensional numerical study of turbulence in an entraining mixed layer,” *Boundary-Layer Meteorol.* **7**, 199-226 (1970).
- ³⁹R. Mikkelsen, “Actuator disk methods applied to wind turbines,” Ph. D. Dissertation (Technical University of Denmark, Copenhagen, 2003).
- ⁴⁰F. Porté-Agel, Y.-T. Wu, H. Lu, and R. J. Conzemius, “Large-eddy simulation of atmospheric boundary layer flow through wind turbines and wind farms,” *J. Wind. Eng. Ind. Aerodyn.* **99**, 154–168 (2011).
- ⁴¹H. Glauert, 1963: Airplane propellers. In *Aerodynamic Theory*, Volume IV, W. F. Durand (ed.). (Springer, New York, 1935).
- ⁴²H. A. Madsen, “A CFD analysis of the actuator disc flow compared to momentum theory results,” *Proceedings of the 10th IEA Symposium on the Aerodynamics of Wind Turbines* (Edinburgh, 1996), pp. 109-124.
- ⁴³J. N. Sørensen, W. Z. Shen, and X. Munduate, “Analysis of wake states by a full-field actuator disc model,” *Wind Energy* **1**, 73–88 (1998).
- ⁴⁴J. N. Sørensen and R. Mikkelsen, “On the Validity of the Blade Element Momentum Method,” *Proceedings of the European Wind Energy Conference Exhibition* (Copenhagen, 2001), pp. 362-366.
- ⁴⁵J. Meyers, and C. Meneveau, “Flow visualization using momentum and energy transport tubes and applications to turbulent flow in wind farms,” *J. Fluid Mech.* **715**, 335–358 (2013).

- ⁴⁶C. Talbot, E. Bou-Zeid E., and J. A. Smith, “Nested mesoscale-large eddy simulations with WRF: performance in real test cases,” *J. Hydrometeorol.* **13**(5), 1421–1441 (2012).
- ⁴⁷J. D. Mirocha, B. Kosović, and G. Kirkil, “Resolved turbulence characteristics in large-eddy simulations nested within mesoscale simulations using the Weather Research and Forecasting model,” *In press at Mon. Wea. Rev.* (2013)
- ⁴⁸M. Courtney, R. Wagner, and P. Lindelow, “Testing and comparison of lidars for profile and turbulence measurements in wind energy,” *IOP Conference Series: Earth and Environmental Science.* **1**, 012021 (2008).
- ⁴⁹M. L. Aitken, M. E. Rhodes, and J. K. Lundquist, “Performance of a wind-profiling lidar in the region of wind turbine rotor disks,” *J. Atmos. Ocean. Tech.* **29**, 347–355 (2012).
- ⁵⁰C. J. Grund, R. M. Banta, J. L. George, J. N. Howell, M. J. Post, R. A. Richter, and A. M. Weickmann, “High-Resolution Doppler Lidar for Boundary Layer and Cloud Research,” *J. Atmos. Ocean. Tech.* **18**, 376–393 (2001).
- ⁵¹R. M. Banta, L.D. Olivier, P.H. Gudiksen, and R. Lange, “Implications of small-scale flow features to modeling dispersion over complex terrain,” *J. Appl. Meteorol.* **35**, 330–342 (1996).
- ⁵²W. Johnson and N. Kelley, “Design Specifications for the Development of the Initial Validation Software (Version 3.0) for Processing of NWTC 80-Meter Meteorological Tower Data,” Report No. NREL/TP-500-27104, National Renewable Energy Laboratory, Golden, CO (2000)

- ⁵³J. Smagorinsky, J., “General circulation experiments with the primitive equations.” *Mon. Wea. Rev.* **91**, 99–152 (1963).
- ⁵⁴A. S. Monin and A. M. Obukhov, “Osnovnye zakonomernosti turbulentnogo peremeshivaniya v prizemnom sloe atmosfery (Basic laws of turbulent mixing in the atmosphere near the ground),” *Trudy geofiz. inst. AN SSSR* **24**(151), 163–187 (1954).
- ⁵⁵S. P. Arya, *Introduction to Micrometeorology*, 2nd ed. (Academic Press, San Diego, 2001).
- ⁵⁶F. Bingöl, J. Mann, and G. C. Larsen, “Light detection and ranging measurements of wake dynamics part I: One-dimensional Scanning,” *Wind Energy* **13**(1), 51–61 (2010).
- ⁵⁷M. E. Rhodes and J. K. Lundquist, “The effect of wind turbine wakes on summertime midwest atmospheric wind profiles,” *Accepted for publication in Boundary-Layer Meteorol.* (2013).
- ⁵⁸T. Burton, N. Jenkins, D. Sharpe, and E. Bossanyi, *Wind Energy Handbook*, 2nd ed. (Wiley, Chichester, 2011).
- ⁵⁹D. Wood, *Small Wind Turbines: Analysis, Design and Application*, (Springer-Verlag, London, 2011).
- ⁶⁰R. C. Aster, B. Borchers, and C. H. Thurber, *Parameter Estimation and Inverse Problems*, 2nd ed. (Elsevier, 2013).
- ⁶¹B. J. Rye, and R. M. Hardesty, “Discrete spectral peak estimation in incoherent backscatter heterodyne lidar. I: Spectral accumulation and the Cramer-Rao lower bound,” *IEEE Trans. Geosci. Remote Sens.* **31**, 16–27 (1993).

FIGURE CAPTIONS

Figure 1. Ten-min average values of U (top), λ (upper middle), T (lower middle) and Ri (bottom), using data at 50 and 2 m, measured between 13:00 and 17:10 MST on April 22, 2011, at various heights from an instrumented tower (M2) and a vertically-profiling lidar (WC) upwind of the turbine. The horizontal dashed lines indicate mean values.

Figure 2. Ten-min average profiles (blue-green) of U (left) and λ (right) from LES using two H_S values, as indicated. The thin, horizontal, gray dotted lines indicate z_H , and the thin, vertical, gray dotted lines show the 80 m WC average value during the time period shown in Figure 1, and $\lambda = 270^\circ$, respectively. The thick black lines show the four-hour average LES values.

Figure 3. Instantaneous U values at z_H at the beginnings of (left) hours 17 and (right) 19, from the (top) weakly and (bottom) moderately convective simulations. The thin, vertical, black dotted line marks the position of the GAD at $x = y = 0D$.

Figure 4. Four-hour averaged velocity components (left: u ; middle: v ; and right: w) at the location of the GAD in the y - z plane from the weakly convective case. The central black dot indicates the GAD center, whereas the black dotted circle shows its perimeter. The gray dotted lines depict the WRF model's grid cells.

Figure 5. Four-hour averaged velocity components (top and middle: u ; bottom: w) at (top and bottom) z_H and (middle) y_H from the weakly convective simulation. The black dotted lines show the position of the GAD in the x - y and x - z planes.

Figure 6. Four-hour averaged velocity deficits (VD) in the (upper) x - y and (lower) x - z planes, at z_H and y_H , respectively. The black dotted lines in the panels show the position of the GAD,

whereas that in the color bar indicates the zero level. Results from both the weakly (Figures 6a and 6c) and moderately (Figures 6b and 6d) convective simulations are shown.

Figure 7. HRDL PPI scans of radial velocity using an elevation angle of 2° . White lines show the turbine location. Four scans are shown, two each occurring during the weakly convective (a and b) and moderately convective (c and d) portions of the time period shown in Figure 1. HRDL's beam intersects the turbine approximately 45 m above the ground, and increases by about 35 m at $x = 10D$.

Figure 8. Velocity deficit (VD) as a function of downstream distance occurring between 13:00 and 17:10 MST on April 22, 2011. The black, bold, central line indicates median observed values, whereas the symmetric shaded error bars represent the standard deviation of the measurements. Mean VD values from the LES of weakly and moderately convective conditions are shown by the blue and red lines, respectively.

Figure A1. Vector wind components and angles used in blade element momentum theory and calculations, as described within the Appendix. The advance angle, ψ , is the sum of the hydrodynamic incidence angle, β_i , and the total blade twist angle, ξ_i . Both β_i and ξ_i depend upon the blade pitch angle φ . Total blade twist angle, ξ_i , is the difference between the local blade twist angle and the blade pitch angle, φ . In our implementation of the GAD, the blade pitch angle is a function of the wind speed, V_1 .

Figure A2. Projection of axial and tangential blade forces F_n and F_t , onto WRF's $[x, y, z]$ coordinate system.